




Dual-band acoustic higher-order topological metamaterial composed of meta-atoms and meta-molecules

Changlin Ding,^{*} Jianbing Shi, Yibao Dong , Yun Bai , Shilong Zhai, and Xiaopeng Zhao[†]
Smart Materials Laboratory, School of Physical Science and Technology, Northwestern Polytechnical University, Xi'an 710129, People's Republic of China

 (Received 24 April 2023; revised 2 August 2023; accepted 25 August 2023; published 11 September 2023)

We present a dual-band topological transport of edge states and corner states in a composite acoustic higher-order topological metamaterial (AHOTM) composed of meta-atoms of hollow tubes (HTs) and meta-molecules of opened-hole hollow tubes (OHTs) arrayed as a regular triangle in a hexagonal lattice with C_{3v} symmetry. The AHOTM has two degenerate Dirac points (DPs) in the high-symmetry point K that are separately tuned by the geometry sizes of HTs and OHTs because of their local resonances and weak interactions. The rotation of HTs and OHTs in a unit cell with an angle of -30° [unit cell A (UCA)] or 30° [unit cell B (UCB)] lifts the degeneracies of the two DPs and produces two entire opened band gaps, in which there are two pairs of topological edge bands. We numerically and experimentally demonstrate topological valley transports of edge states for the AHOTM in two bands. The AHOTM presents frequency-selective topological transport of edge states by rotating one structure and can sustain the topologically robust edge states against some defects. In the two frequency regions, higher-order corner states are also observed in the vertices of the triangular UCB array surrounded by the UCA array, which can also realize frequency-selective higher-order corner states by rotating one structure. This study may pave a feasible way to design multiband and broadband acoustic topological insulators for their flexible manipulation of sound waves.

DOI: [10.1103/PhysRevB.108.094103](https://doi.org/10.1103/PhysRevB.108.094103)

I. INTRODUCTION

Topological transport with defect immunity, backscattering immunity, and robust edge states is the extension of quantum Hall, quantum spin Hall, and quantum valley Hall effects and enriches the study of condensed matter physics [1–4]. The topology is firstly realized in electronic systems by introducing a magnetic field to break the time-reversal symmetry and then develops into topological insulators, semimetals, and so on [3–8], which have a parallel development in other fields of photonics [9,10], acoustics [11–20] and mechanics [21–26]. Recently, there has been significant progress in the manipulation of acoustic waves via acoustic topology. Analogous to the quantum Hall effect, a circulating fluid flow is utilized to break the time-reversal symmetry to obtain acoustic topological insulators (ATIs) [11]. He *et al.* expand and compress two-dimensional honeycomb arrays of metallic rods to realize acoustic pseudospin states and topological transport [18], which are mimicking the quantum spin Hall effect. This kind of ATI without an external field has a potential application. Although some ATIs have been achieved by phononic crystals based on Bragg scattering, the narrow work frequency band related to the lattice constant limits their applications. Acoustic metamaterials (AMs) [27–30] based on local resonance are another kind of candidate for the design of ATIs. The topological band can be realized in the local resonant frequency region

of AMs determined by their geometry sizes, which means that the AMs provide more possibilities for designing ATIs. Now the designed acoustic topological metamaterials present subwavelength tunable and reconfigurable topological states [31–33].

Although topological insulators (TIs) provide some unique properties for matter waves' manipulation, a d -dimensional TI only transmits gapless nonscattering boundary states in $d-1$ dimensions. A higher-order TI (HOTI) with valley states broadens the band of the topological transport [12]. As a new type of TI, the HOTI can realize boundary states and corner states in lower dimensions. For example, a three-dimensional (3D) HOTI may have higher-order gapped one-dimensional (1D) hinge states and in-gap zero-dimensional (0D) corner states. The corner states or hinge states are topology protected and cannot be removed by external perturbations. The HOTI with rich band dispersions offers many research opportunities [19,20]. The gapless band of HOTIs fabricated by AMs with edge states or corner states is related to local resonance which can be tuned by the geometry sizes of the unit cell. Although the resonant structure solves the tunability of the HOTIs, it cannot broaden the bandwidth of work frequency. Even though some multiband HOTIs can be realized by one structure with many band gaps, the different bands have a fixed frequency relationship [34]. In this paper, we propose a dual-band composite acoustic higher-order topological metamaterial (AHOTM) based on the concepts of local resonance and weak interaction. The AHOTM composed of a two-dimensional (2D) meta-atoms and meta-molecules array presents two isolated degenerate Dirac points (DPs) that can

^{*}dingchanglin@nwpu.edu.cn

[†]xpzha@nwpu.edu.cn

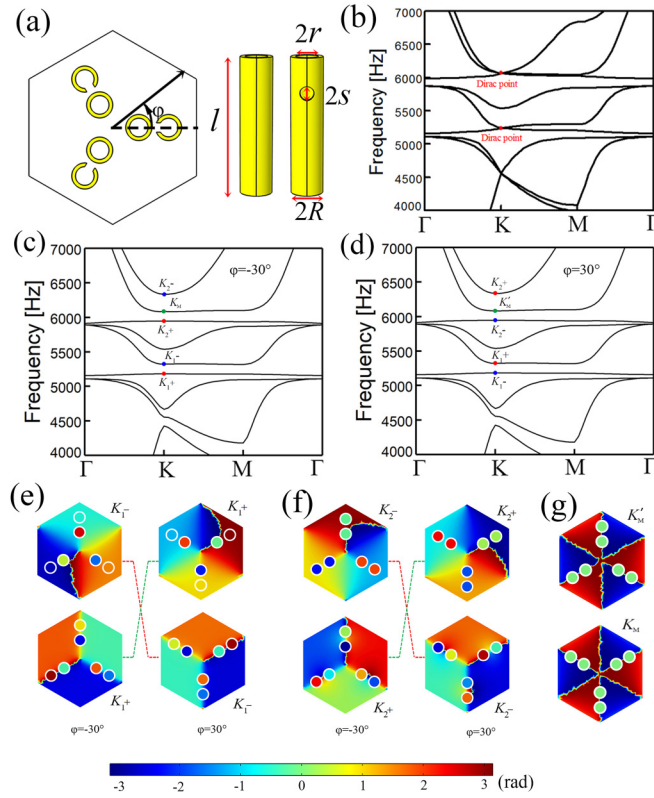


FIG. 1. (a) Schematic diagram of a unit cell of acoustic higher-order topological metamaterial (AHOTM). The band dispersion in AHOTM with different rotation angle (b) $\varphi = 0^\circ$, (c) $\varphi = -30^\circ$, and (d) $\varphi = 30^\circ$. The acoustic pressure phase distribution of the (e) K_1 state, (f) K_2 state, and (g) K_M state.

be tuned by their geometry sizes. By rotating the structures, the AHOTM can realize dual-band 1D edge states and 0D corner states with topological phase transitions. This method provides a feasible and flexible path to design multiband or broadband HOTIs.

II. MODEL ANALYSIS

The selected meta-atom is a hollow tube (HT) with negative mass density and the meta-molecule is an opened-hole hollow tube (OHT) with simultaneously negative mass density and negative modulus from the preliminary studies [29,35]. The meta-molecule of an OHT is considered as the coupling of two meta-atoms of the hollow tube (the tube) and the split hollow sphere (the opened hole and the cavity in the tube). The composite AHOTM is fabricated by HTs and OHTs forming a man-made honeycomb lattice with C_{3v} symmetry. The sectional schematic of a unit cell is shown in Fig. 1(a) and the HT possesses the tube length $l = 30$ mm, the inside radius $r = 2.5$ mm, and the outside radius $R = 3.5$ mm. The OHT is fabricated by drilling a side hole with a radius of $s = 1.5$ mm on the $1/4$ tube of the HT. Both the HTs and the OHTs are arrayed as a regular triangle in a hexagonal lattice with a lattice constant $a = 45$ mm. The φ is the rotated angle of the regular triangle of HTs or OHTs around the Z axis in the center. The HTs are closer to the rotation axis with a distance of 10 mm and the OHTs are 18 mm apart from the center of the unit cell.

The software COMSOL MULTIPHYSICS is conducted to simulate the energy band of the dual-band AHOTM. The material of the meta-atom HTs and meta-molecule OHTs are set as acrylic plastic and the rest of the 3D hexagonal prism cell is filled with air. The mass density of air is $\rho_0 = 1.21$ kg/m³ and the sound velocity is $c_0 = 340$ m/s. The six surfaces of the unit cell are set as the Floquet periodic boundary condition. As the impedances of the meta-atom and meta-molecule are much larger than that of air, the interface between each other can be considered as a rigid boundary.

In the module of pressure acoustics, the eigenmodes are studied to obtain the dispersion of the composite AHOTM along the high-symmetry path Γ - K - M - Γ of the first Brillouin zone (BZ) as shown in Fig. 1(b). Considering the rules of the quantum system, the eigenstates of the K point in the first BZ have two 2D irreducible representations. When the rotated angle φ is 0° , there are two double-degenerate DPs at the symmetry point K of the first BZ. The K_1 state and the K_2 state separately indicate the first and the second DP, which locate at the frequencies of 5242 and 6083 Hz, respectively. The simultaneous rotations of two regular triangles of meta-atoms and meta-molecules will break the mirror symmetry of the unit cell. The corresponding perturbation lifts the degeneracy of the extreme energy in two DPs, which will be opened as two entire valley band gaps. When the composite structure is rotated at an angle of -30° (clockwise direction), the two band gaps with maximum band width appear at the frequency regions of DPs shown in Fig. 1(c) and the structure is labeled as UCA. If the rotated angle is 30° (anticlockwise direction), two opened band gaps are also observed in the dispersion spectra as shown in Fig. 1(d) and the structure is labeled as UCB.

From the acoustic pressure phase distribution of UCA in Figs. 1(e) and 1(f), the phases of the K_1 - and K_2 - states in higher frequencies vary from $-\pi$ to π in clockwise direction, and the phases of the K_1+ and K_2+ states in lower frequencies rotate in the opposite direction, which means sound pseudospin. However, the frequencies of the K_1 - and K_2 - states in UCB are lower than those of the K_1+ and K_2+ states from Figs. 1(e) and 1(f), thereby demonstrating band inversions and topological transition in the two frequency regions. We note that there is an invariable energy band in the second band gap. Figure 1(g) indicates the phase of point K_M ($\varphi = -30^\circ$) and K'_M ($\varphi = 30^\circ$) of the middle band with alternative $-\pi$ and π distribution meaning that there is not a sound pseudospin in this band, which indicates that this middle band is a normal bulk band and may lead to the second topological band being narrower.

III. RESULTS AND DISCUSSION

The topological properties associated with bands above and below gaps can be characterized by the study of the so-called Berry-Pancharatnam-Zak phase, which is obtained by the following closed path L_0 integral:

$$\phi_n = \oint_{L_0} \mathbf{A}_n(\mathbf{k}) \cdot d\mathbf{k}, \quad (1)$$

where $\mathbf{A}_n(\mathbf{k})$ known as the Berry connection is defined as

$$\mathbf{A}_n(\mathbf{k}) = i \langle u_n(\mathbf{k}) | \nabla_{\mathbf{k}} | u_n(\mathbf{k}) \rangle. \quad (2)$$

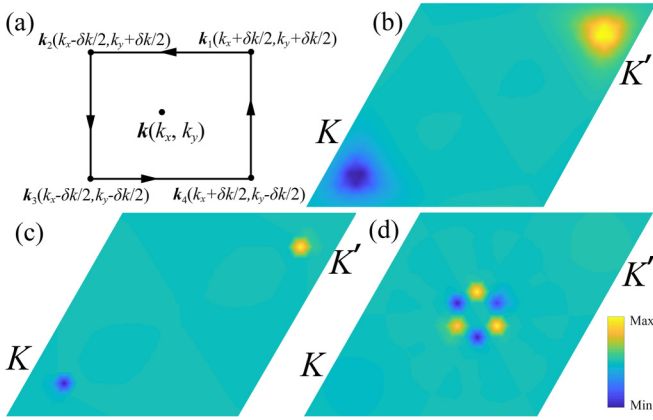


FIG. 2. (a) The schematic diagram of Berry curvature calculation. The calculated Berry curvature of the unit cell B in the lower band of the first band gap (b), second band gap (c), and the middle band of the second band gap (d).

$u_n(\mathbf{k})$ is the eigenstate of a point \mathbf{k} in reciprocal space. It is known that the Berry-Pancharatnam-Zak phase is gauge invariant up to multiples of 2π and depends only on the geometry of the path L_0 , whereas the Berry connection is gauge dependent. An important gauge-independent quantity is the Berry curvature $\Omega_n(\mathbf{k})$.

$$\Omega_n(\mathbf{k}) = \nabla_{\mathbf{k}} \times \mathbf{A}_n(\mathbf{k}). \quad (3)$$

From Stokes' equation, we can obtain

$$\begin{aligned} \phi_n &= \oint_{L_0} \mathbf{A}_n(\mathbf{k}) \cdot d\mathbf{k} = \iint_{S_0} \nabla_{\mathbf{k}} \times \mathbf{A}_n(\mathbf{k}) \cdot d\mathbf{S} \\ &= \iint_{S_0} \Omega_n(\mathbf{k}) \cdot d\mathbf{S}. \end{aligned} \quad (4)$$

There is a numerical method to calculate Berry curvature. We choose a square area with a side length of δk around a point \mathbf{k} in reciprocal space that is much smaller than the first Brillouin zone. The wave vectors of four square vertices are $\mathbf{k}_1, \mathbf{k}_2, \mathbf{k}_3$, and \mathbf{k}_4 as shown in Fig. 2(a) [36,37]. The scalar Berry curvature of the point \mathbf{k} can be calculated as follows:

$$\begin{aligned} \Omega_n(\mathbf{k}) &= -\text{Im}[\langle u_n(\mathbf{k}_1) | u_n(\mathbf{k}_2) \rangle + \langle u_n(\mathbf{k}_2) | u_n(\mathbf{k}_3) \rangle \\ &\quad + \langle u_n(\mathbf{k}_3) | u_n(\mathbf{k}_4) \rangle + \langle u_n(\mathbf{k}_4) | u_n(\mathbf{k}_1) \rangle] / (\delta k)^2. \end{aligned} \quad (5)$$

The eigenstate $u_n(\mathbf{k}_1)$ can be retrieved from pressure distribution of the primitive cell under the simulation of an acoustic ‘‘eigenfrequency’’ module. Figures 2(b) and 2(c) demonstrate the Berry curvature of the first and second band gaps of UCB, which presents yellow (blue) points near the K and K' points representing the upward (downward) peaks, meaning valley Hall phases. The valley Chern number (VCN) near the K point can be calculated as

$$C_K = \iint_{BZ} \Omega_n(\mathbf{k}) \cdot d^2k. \quad (6)$$

From Fig. 2 and Eq. (6), the VCN near the point K is separately calculated about -0.48 and -0.47 for the lower band of first and second band gap of UCB. Similarly, the VCN of UCA is calculated as 0.48 and 0.47 for the first and second band, respectively. Therefore, the UCA and UCB

present different VCNs near $1/2$ and $-1/2$ in the first and the second band gap, which indicates different valley topologies. From the calculated Berry curvature in Fig. 2(d), the VCN for the middle band of the second band gap in UCB is near -0.75 .

Furthermore, the topologies of UCA and UCB can also be explained by the $\mathbf{k} \cdot \mathbf{p}$ perturbation theory. The effective Hamiltonian near the DP can be expressed as

$$H_K = v_D(\delta k_x \sigma_x + \delta k_y \sigma_y) + \Delta_g \sigma_z, \quad (7)$$

where v_D is the Dirac velocity of the conic dispersion at $\varphi = 0^\circ$, and δk_x and δk_y are the momentum deviations from the K point. σ_x , σ_y , and σ_z are Pauli matrices,

$$\Delta_g = (\omega_{K_+} - \omega_{K_-})/2. \quad (8)$$

where ω_{K_+} is the frequency of the K_+ state and ω_{K_-} is the frequency of the K_- state. Δ_g has the same absolute values but opposite signs under the rotated angles of $\varphi = 30^\circ$ and $\varphi = -30^\circ$. The Berry curvatures are calculated by a Hamiltonian as

$$\Omega(H_K) = \frac{1}{2}(\Delta_g/v_D)(\delta k^2 + \Delta_g^2/v_D^2)^{-3/2}. \quad (9)$$

The VCN of the K point can be obtained by the integration of Berry curvatures

$$C_{K,K'} = \int \Omega(\delta k_x, \delta k_y) d^2k / 2\pi = \text{sgn}(\Delta_g)/2. \quad (10)$$

From the expression of topological charge, the value of C_K should only be $0, 1/2$, or $-1/2$. When the rotated angle in the AHOTM is -30° and 30° , the value of topological charge C_K is separately $-1/2$ and $1/2$ in the two pairs of valley bands. The different directional rotations in the composite AHOTM exhibit opposite signs of topological charges, which obviously present different valley topologies.

To further confirm that the first and second DPs in the dispersion spectra are respectively determined by the acoustic meta-atoms and meta-molecules, the degeneracies of the two DPs are investigated by changing the rotation angle φ of the single structures. From Fig. 3(a), when a regular triangle of meta-atoms of HTs in each unit cell is rotated from -60° to 60° with a step of 2° and the meta-molecules of OHTs remain stationary, the first DP firstly gradually opens and reaches maximum band gap at -30° , and then it will slowly close and become a point at 0° . As the rotated angle increases from 0° to 60° , a repeated process will happen on the first DP. However, the second DP maintains degeneracy with a slight frequency change. Similarly, by only rotating the OHTs from -60° to 60° with a step of 2° , it is shown in Fig. 3(b) that the second DP experiences the processes of ‘‘open-close-reopen,’’ in which the width of the opened band gap reaches maximum at the angle of -30° and 30° , but the first DP maintains degeneracy. The degeneracy points in different angles are not folded perfectly because of the weak interaction between the meta-atoms and meta-molecules. It is further demonstrated that the first and second DPs are attributed to the HT arrays and OHT arrays, respectively, and the two structures have weak interaction in the topological band. The meta-atom HT and meta-molecule OHT are local resonant structures and the DP frequency can be tuned by the geometry sizes. From Fig. 3(c), the DP may cover the frequency range of $5000\text{--}9800$ Hz by varying the tube length l of the HT and the OHT from 10 mm

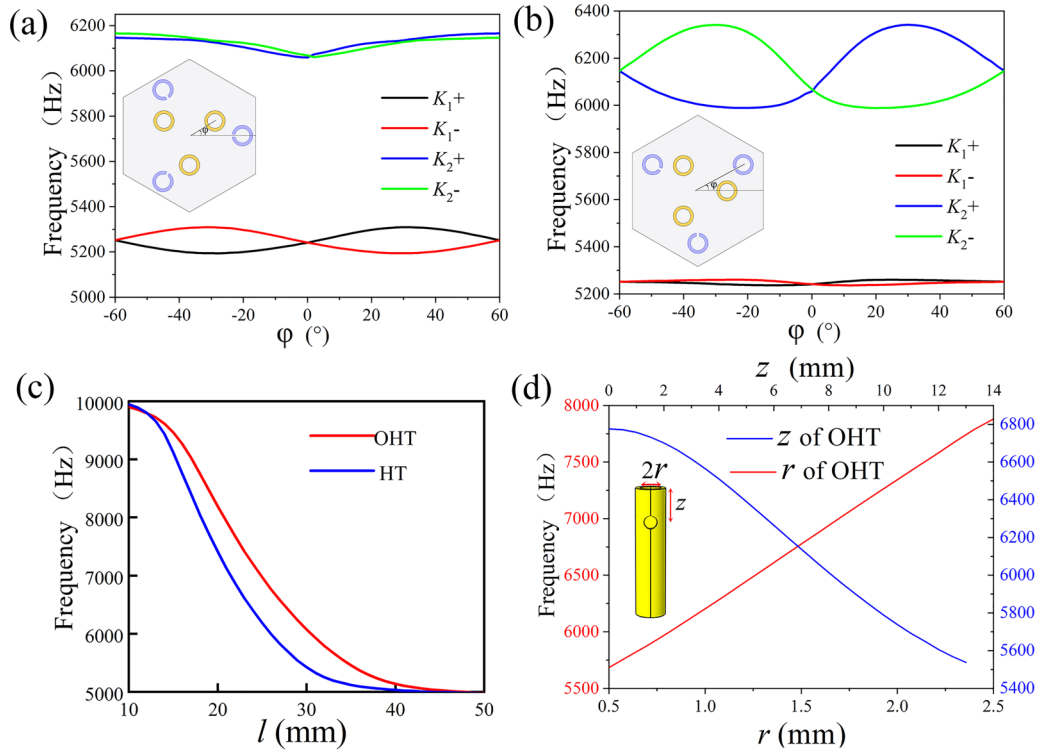


FIG. 3. The relationship between the valley frequency of the K point and the rotation angle ϕ in the case of (a) only rotating the meta-atom structure and (b) only rotating the meta-molecule structure. (c) The relationship between DP frequency and the tube length of the HT and the OHT. (d) The DP frequency of the OHT structure with different radius s and location z of the opened hole.

to 50 mm but with other geometry parameters unchanged. The DP can be also moved to a higher frequency band via the increase of the opened-hole radius of the OHT, while it will generate a frequency shift to a lower band when the opened hole moves up to the center of the OHT [Fig. 3(d)]. The weak interaction and tunable DP band of a composite AHOTM may be suitable to realize broadband ATIs.

Given that an interface composed of two lattices with different VCNs produces a topology-protected edge state, which is scattering immune, defect immune and transport robust, a supercell is designed by alternatively arranging a 6×2 UCA array and a 6×2 UCB array to confirm the existence of the edge state. Three groups of faces in a parallelepiped supercell are set as Floquet periodical boundaries. Figure 4(a) is the band dispersion of the supercell, where the shaded part indicates bulk state with valley point and the red and blue curves are edge states. The red curves are the edge states that transmit along the interface of UCA/UCB (defined as I1) and the blue curves indicate the edge transmission along the interface of UCB/UCA (defined as I2). The edge states of I1 distribute in two frequency regions of 5200–5310 and 6020–6100 Hz and those of I2 locate at two bands of 5210–5310 and 6001–6020 Hz. It is noted that there is an additional edge band for each structure (I1 and I2) in the two complete band gaps [34,38]. Two pairs of edge states for I1 (M_1 and M_2) and I2 (N_1 and N_2) in the first band and two pairs of edge states for I1 (C_1 and C_2) and I2 (D_1 and D_2) in the second band are selected to investigate the topological transport. From the absolute pressure distribution shown in Figs. 4(b) and 4(c), the most energy concentrates on the interfaces of I1 and I2 for all the edge

states. In comparison, the topological transport energy of edge states C_2 , D_2 , M_2 , and N_2 is stronger than that of C_1 , D_1 , M_1 , and N_1 . Figure 4(b) demonstrates that a lot of resonant energy is localized in the OHT for the weaker edge states (C_1 and D_1) and concentrates in the OHT and HT for the stronger edge states (C_2 and D_2) in the second band gap. Therefore, one pair of edge states (C_1 and D_1) is attributed to the local resonance of the OHT and the other (C_2 and D_2) arises from the local resonance and coupling effect of the OHT and HT in the second topological band. Similarly, one pair of edge states (M_1 and N_1) is attributed to the local resonance of the HT and the other (M_2 and N_2) is due to the local resonance and coupling effect of the OHT and HT in the first topological band.

In COMSOL simulations, we design a topological interface of I1. A point source is placed on the left port of I1. Figures 5(a) and 5(b) separately show the absolute pressure distribution of the composite AHOTM interface at the first topological band of 5230 Hz and the second of 6060 Hz. It is shown that the acoustic energy only propagates along the interface between the UCA array and the UCB array and attenuates sharply in the bulk space of the lattice demonstrating the topological transports of edge states. There is a lot of energy in the tube of the unit cell, which is due to the local resonance of HTs and OHTs.

To illustrate the reliability of the simulations, an experiment is carried out to measure the topological transport of edge states. The sample is fabricated by 3D printing technology. A template is firstly printed using plastic material, and then all the HTs and OHTs are inserted into the template as shown in Fig. 5(c). The topology of the presented material

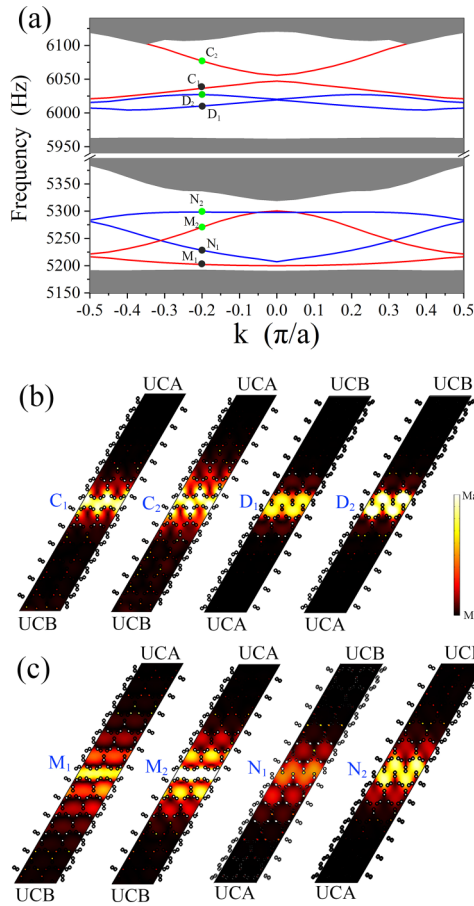


FIG. 4. (a) The band dispersion of a supercell composed of unit cell A (UCA) and unit cell B (UCB) arranged together along the direction of ΓK . The acoustic pressure distribution of the supercell in (b) the second topological band and (c) the first topological band.

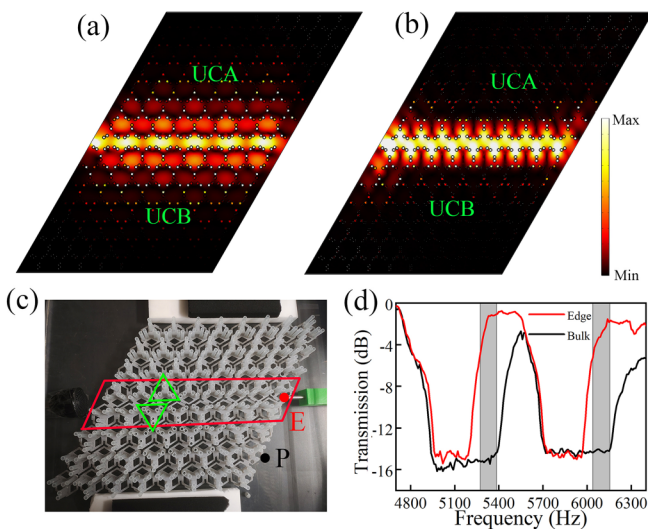


FIG. 5. The simulated topological transport of edge states in interface 1 (I1) at (a) the first band of 5230 Hz and (b) the second band of 6060 Hz. (c) The diagram of experimental measurement of edge states in a topological waveguide. (d) The tested curves of edge state and bulk state.

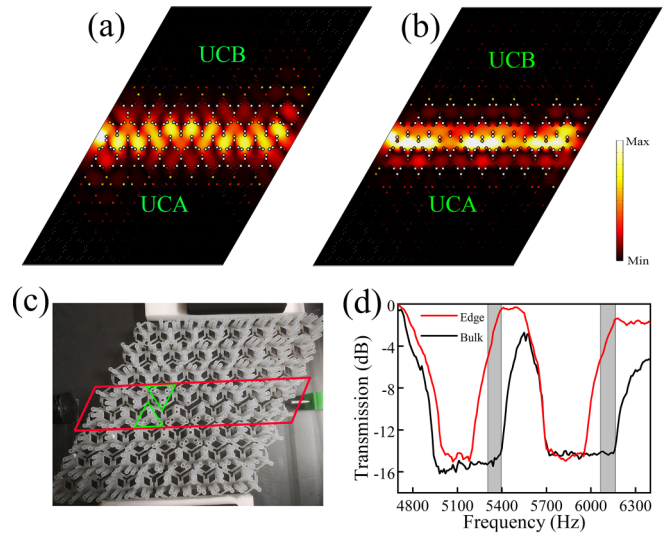


FIG. 6. The simulated topological transport of edge states in interface 2 (I2) at (a) the first band of 5230 Hz and (b) the second band of 6015 Hz. (c) The diagram of experimental measurement of edge states in I2. (d) The tested curves of edge state and bulk state.

is mainly attributed to the local resonance of microstructures (the air oscillating in and out of the HTs and OHTs) and the lattice symmetry. The plastic template is a frame with a thickness of 3 mm and is used to fasten the HTs and OHTs in the experiment, which will rarely affect the local resonance of microstructures. Therefore, the plastic template has little influence on the topological transport of the materials.

There are two parts in the sample as a waveguide. The top of the interface is a periodical array composed of UCAs with a nonzero topological charge and the bottom is also a periodical UCB array with an opposite topological charge. The sample is measured in a plane waveguide consisting of two parallel acrylic plates. To establish an anechoic environment, some sound-absorbing foams are filled on the boundaries of the plates. A sound source (BMS 4512ND) driven by an integrated sound card is placed at the front of the interface in the sample and a 1/4-inch microphone (MPA 416) is used to measure the transmitted sound at the other side of the sample. In the experiment, the measurements of the red point E and the black point P represent the transmission of the edge state and the bulk state, respectively. After the postprocessing of tested signals in an oscilloscope, the experimental transmission curves are obtained as shown in Fig. 5(d). The black and red lines denote the transmission of the bulk state and edge state, respectively. It is indicated that there is a transmission enhancement of 16 dB for the edge states compared with the bulk states in the two gray regions of 5302–5395 and 6064–6162 Hz, that is, the edge states can efficiently transmit through the interface with topological phase transition and the bulk states are forbidden, which just locate in the two valley bands of the composite AHOTM. The difference between the simulation and experiment may be because of mechanical error. Similarly, the simulated and experimental results also demonstrate the topological transport of I2 as shown in Figs. 6(a)–6(d). From Figs. 5(d) and 6(d), it is noted that the high edge transmission covers a frequency region of

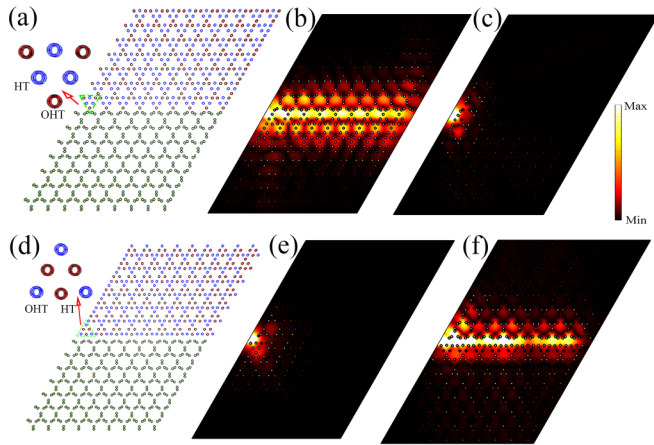


FIG. 7. The frequency-selective topological transport of edge states in the first band (a)–(c) and the second band (d)–(f). (a) and (d) separately indicate the sectional diagram of I1 with rotation of the OHT and HT in UCA. (b), (e) The acoustic field distribution at 5230 Hz. (c), (f) The acoustic field distribution at 6060 Hz.

the bulk states' forbidden band and passband. The topological edge transmission reaches maximum values in the passband of bulk states, which may be attributed to a superposition of bulk states and edge states.

As the AHOTM has two isolated topological bands, it can be used to realize frequency-selective topological transport of edge states. By rotating the OHT of UCA (marked in red) at an angle of 60° (anticlockwise direction) for the interface I1 [Fig. 7(a)], the second topological band will be switched off. The sound energy transmits along the interface I1 in the first topological band near 5230 Hz shown in Fig. 7(b) and is forbidden in the second band near 6060 Hz in Fig. 7(c). By rotating the HT of UCA (marked in red) at an angle of

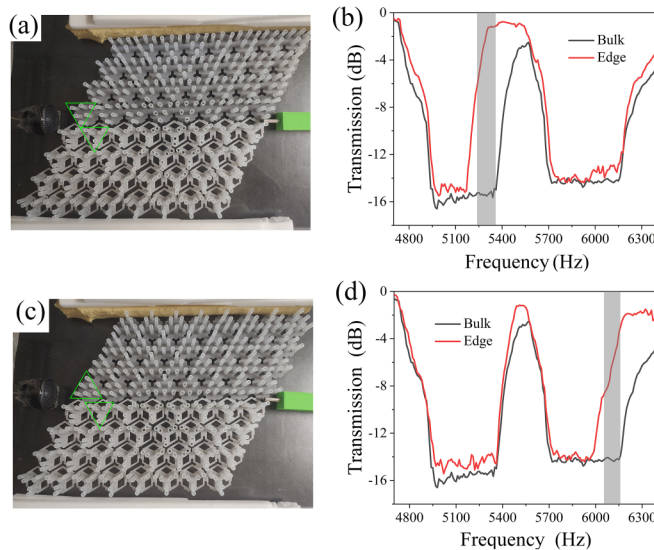


FIG. 8. (a) The diagram of experimental measurement and (b) tested curves of edge state and bulk state for I1 with a 60° -rotated OHT in UCA. (c) The diagram of experimental measurement and (d) tested curves of edge state and bulk state for I1 with a 60° -rotated HT in UCA.

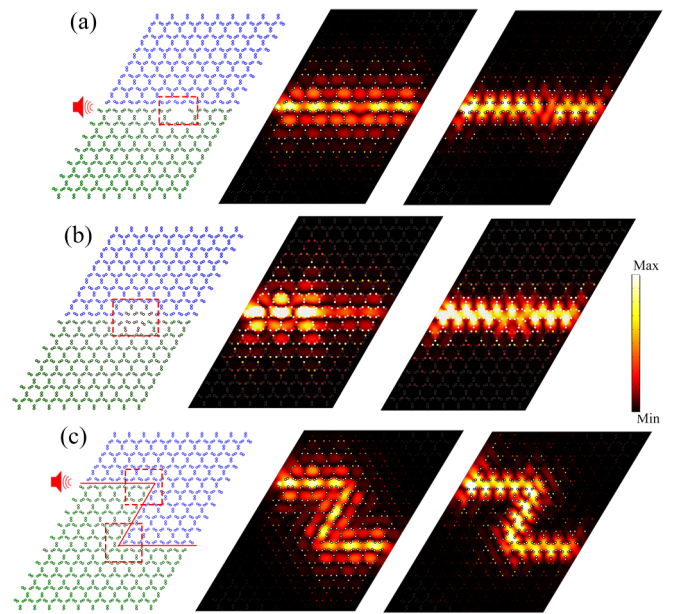


FIG. 9. The one-way transmission of robustness against defects in the AHOTM composed of UCA (blue structure) and UCB (green structure). The left panels indicate waveguide samples; the right two groups of panels separately show the calculated pressure intensity distributions in two topological bands of 5230 and 6060 Hz (a) with cavity, (b) with disorder, and (c) with sharp turns.

60° (anticlockwise direction) for interface I1 [Fig. 7(d)], the first topological band will be switched off. The sound energy transmits along interface I1 in the second topological band of 6060 Hz [Fig. 7(f)] and is forbidden in the first band of 5230 Hz [Fig. 7(e)]. Therefore, by rotating the OHTs or HTs, interface I1 can realize frequency-selective topological transport of edge states near 5230 and near 6060 Hz.

To further illustrate the tunable control on edge states, an experiment is conducted to measure the topological transport of interface I1 with the rotated structure. Figure 8(a) is the fabricated interface I1 with a 60° -rotated OHT in UCA and the measured environment is similar to that in Fig. 5(c). Compared with the results in Fig. 5(d) (dual-band edge states), the transmission curve of bulk state shown in Fig. 8(b) also demonstrates two band gaps. The transmission of edge state indicates that an obvious transmission enhancement only exists in the first band gap and disappears in the second gap. That is to say, the second edge state can be switched off by rotating the OHT in UCA of I1. Similarly, Fig. 8(c) is the fabricated interface I1 with a 60° -rotated HT in UCA and the transmissions of bulk state and edge state indicate that the transmission enhancement only appears in the second band gap and vanishes in the first gap. The first edge state can be switched off by rotating the HT in UCA. Therefore, it is experimentally illustrated that the first and the second topological transport of edge states can be independently tuned by rotating HTs or OHTs in the UCA of I1.

The robustness of edge states against defects is a very surprising property of ATIs. A series of defects including unit cavity, disorder, and sharp turns are introduced to our dual-band topological protected waveguide of I1 to investigate the robustness of edge states. The left panels in Figs. 9(a)–9(c)

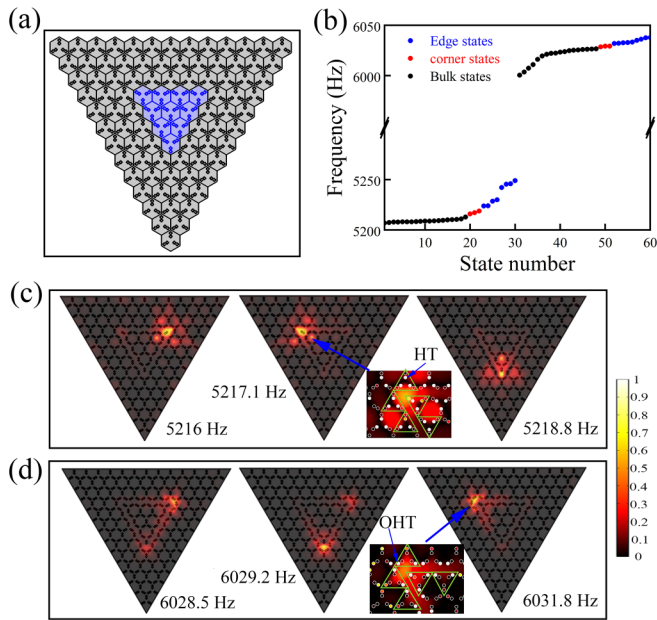


FIG. 10. (a) Triangular structure constructed by the UCB array surrounded by the UCA array. (b) The eigenfrequency diagram calculated from the triangular structure. Sound pressure distribution of corner states in the first band gap (c) and the second band gap (d).

are the cross-sectional diagrams of numerical models (II) for simulation with three different defects and the right two panels demonstrate the distributions of simulated pressure intensity in two topological bands, in which II with the defects of unit cavity, disorder, or sharp turns presents a topology-protected transport along the interface of UCA/UCB with little energy in the bulk space. From Fig. 9(b), there is an obvious sound attenuation when the energy transmits through two pairs of disorder unit cells in the first band. If the disorder defects are large, the topological transport along II will disappear. Therefore, the AHOTM presents a robustness of edge propagation in two topological bands for some little defects, but the topology of AHOTM will be affected by some large defects.

Considering that an edge state with a gap may produce a higher-order topological state at lower dimensions. A higher-order corner state can be found in the gap of the edge state in valley TIs. According to the expanded bulk-boundary correspondence, the topological protected 0D corner state may appear in the corner point of the 2D AHOTM. In Fig. 10(a), we present a triangular supercell composed of a triangular UCB lattice surrounded by a UCA lattice. The eigenfrequency of the structure calculated by COMSOL [Fig. 10(b)] demonstrates that there is a gap between edge states (blue point) and bulk states (black point), which supports a corner state (red point). According to the distribution of the acoustic pressure in Fig. 10(c), most of the energy concentrates on the three corner points of the triangle lattice at 5216, 5217.1, and 5218.8 Hz in the first band gap, which demonstrates corner states in the structure. For the second band gap, the energy also focuses on the corner points of the triangle lattice in the frequencies of 6028.5, 6029.2, and 6031.8 Hz shown in Fig. 10(d). Therefore, there are two groups of corner states in the composite AHOTM. Actually, three corner states in two bands should

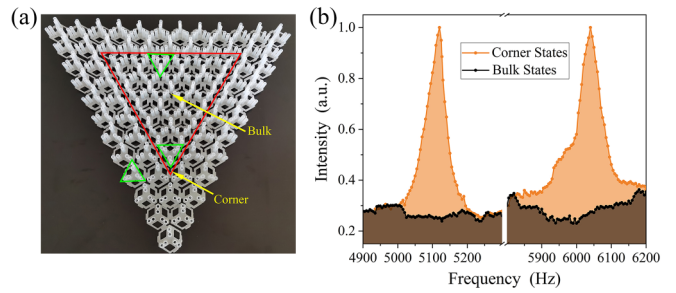


FIG. 11. (a) Diagram of the experimental sample for corner state measurement. (b) Normalized transmitted sound spectra at corner and bulk points.

be degenerate. The fact that the three corner states are not in the same eigenfrequency [39,40] with a difference of 1–2 Hz maybe attributed to the convergence error in the COMSOL simulation. To clearly distinguish the pressure distribution of corner states, the insets show that the energy of the first corner states concentrates in the meta-atoms of HTs (inner cells of the marked green triangle) from Fig. 10(c) and the energy of the second corner states focuses on the meta-molecules of OHTs (outer cells of the marked green triangle) from Fig. 10(d). Therefore, the emergence of the first and second corner states is separately attributed to the HTs and OHTs.

Based on the above-mentioned simulated results, an experimental sample is fabricated by 3D printing technology as shown in Fig. 11(a). The red line insulates two kinds of lattices with different topologies. The red triangle region is composed of the UCB array, and the other areas are filled with the UCA array. A loudspeaker and a 1/4-inch microphone are separately placed above and below the corner point of the red line. When a sound wave is incident on the corner point, the transmitted signal can be received by the microphone. For comparison, a bulk point in the area of the UCB array shown in Fig. 11(a) is selected to measure the transmission of bulk state. The normalized sound intensity is plotted in Fig. 11(b), which demonstrates that the transmitted intensity of bulk state is very low, but the corner state presents two sharp peaks near the predicted frequencies. It is experimentally proved that the composite AHOTM supports dual-band topological transport of corner states.

The AHOTM with two isolated topological bands can also realize a frequency-selective higher-order corner state. For the dual-band triangular AHOTM [Fig. 11(a)], by rotating the OHT of UCA (marked in green) at an angle of 60°, supercell A is fabricated as shown in Fig. 12(a). The calculated eigenfrequency of the structure [Fig. 12(b)] indicates that the topological corner states and edge states disappear in the second band gap. The corner states (red points) only appear in the first gap between edge states (blue points) and bulk states (black points). That is to say, the second topological band with edge states and corner states is switched off. From the experimental measurement, the transmission of bulk state of supercell A is very low and the transmission of corner state presents only a sharp peak near the first band gap and the second peak disappears, which means that the second corner state disappears. By rotating the HT of UCA (marked in green) at an angle of 60°, supercell B is fabricated as shown

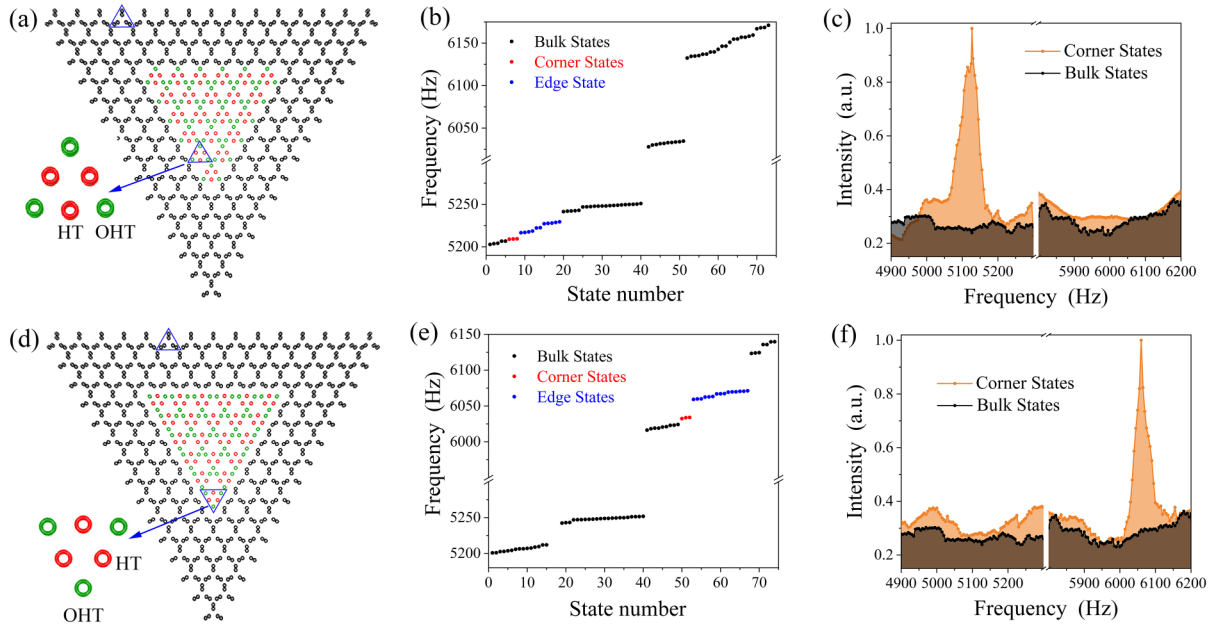


FIG. 12. Diagram of (a) supercell A (inset is the structure of UCA with a 60° -rotated OHT) and (d) supercell B (inset is the structure of UCA with a 60° -rotated HT). The calculated eigenfrequency of (b) supercell A and (e) supercell B. The measured transmissions of bulk state and corner state for (c) supercell A and (f) supercell B.

in Fig. 12(d). The eigenfrequency of the structure [Fig. 12(e)] indicates that the corner states (red points) only appear in the second gap between edge states (blue points) and bulk states (black points), but they disappear in the first band gap, which means that the first topological band with edge states and corner states is switched off. From the experimental measurement shown in Fig. 12(f), supercell B only presents a corner state near the second band gap and the first corner state disappears. Therefore, it is demonstrated that the two corner states can be independently tuned by rotating the OHT or the HT of UCA in the dual-band AHOTM.

IV. CONCLUSION

In summary, we have demonstrated a subwavelength composite AHOTM composed of negative-mass meta-atoms of HTs and double-negative meta-molecules of OHTs analogous to quantum valley Hall effect with two DPs in the high-symmetry point K . The first DP is determined by the HTs array and the second is attributed to the OHTs array. The rotations of structure in the unit cell with the angles of -30° (UCA) and 30° (UCB) both open the DP as an entire band gap and generate energy band reversion at the K point with

topological phase transition in the two bands. The AHOTM waveguide supports the topology-protected transport of edge state along I1 and I2 at two frequency regions. The AHOTM also presents frequency-selective topological transport of edge states by rotating one structure and can sustain the topologically robust edge states against some defects. The supercell composed of a triangular UCB array surrounded by a UCA array presents corner states in the triangle vertices in the two band gaps. The two corner states can also be independently tuned by rotating the HT or OHT of UCA in the triangular supercell. Therefore, our proposed composite AHOTM has realized dual-band edge states and higher-order corner states. Considering that the meta-atoms and meta-molecules in the AHOTM have weak interaction and can tune the topological bands by changing geometry sizes, the broadband AHOTM may possess an exciting prospect.

ACKNOWLEDGMENT

This work was supported by National Natural Science Foundation of China (Grants No. 52272306 and No. 11764033) and the Aeronautic Science Foundation of China (Grant No. 2018ZF53071).

- [1] K. v. Klitzing, G. Dorda, and M. Pepper, New Method for High-Accuracy Determination of the Fine-Structure Constant Based on Quantized Hall Resistance, *Phys. Rev. Lett.* **45**, 494 (1980).
- [2] R. B. Laughlin, Anomalous Quantum Hall Effect: An Incompressible Quantum Fluid with Fractionally Charged Excitations, *Phys. Rev. Lett.* **50**, 1395 (1983).

- [3] M. Z. Hasan and C. L. Kane, *Colloquium*: Topological insulators, *Rev. Mod. Phys.* **82**, 3045 (2010).
- [4] X. L. Qi and S. C. Zhang, Topological insulators and superconductors, *Rev. Mod. Phys.* **83**, 1057 (2011).
- [5] C. L. Kane and E. J. Mele, Quantum Spin Hall Effect in Graphene, *Phys. Rev. Lett.* **95**, 226801 (2005).

- [6] B. A. Bernevig, T. L. Hughes, and S. C. Zhang, Quantum spin Hall effect and topological phase transition in HgTe quantum wells, *Science* **314**, 1757 (2006).
- [7] N. P. Armitage, E. J. Mele, and A. Vishwanath, Weyl and Dirac semimetals in three-dimensional solids, *Rev. Mod. Phys.* **90**, 015001 (2018).
- [8] M. Z. Hasan, G. Chang, I. Belopolski, G. Bian, S. Y. Xu, and J. X. Yin, Dirac and high-fold chiral fermions in topological quantum matter, *Nat. Rev. Mater.* **6**, 784 (2021).
- [9] K. Fang, Z. Yu, and S. Fan, Realizing effective magnetic field for photons by controlling the phase of dynamic modulation, *Nat. Photon.* **6**, 782 (2012).
- [10] A. B. Khanikaev, S. H. Mousavi, W. K. Tse, M. Kargarian, A. H. MacDonald, and G. Shvets, Photonic topological insulators, *Nat. Mater.* **12**, 233 (2013).
- [11] R. Fleury, D. L. Sounas, C. F. Sieck, M. R. Haberman, and A. Alù, Sound isolation and giant linear nonreciprocity in a compact acoustic circulator, *Science* **343**, 516 (2014).
- [12] B. Y. Xie, H. X. Wang, X. J. Zhang, P. Zhan, J. H. Jiang, M. H. Lu, and Y. F. Chen, Higher-order band topology, *Nat. Rev. Phys.* **3**, 520 (2021).
- [13] R. Xue, Y. Yang, and B. Zhang, Topological acoustics, *Nat. Rev. Mater.* **7**, 974 (2022).
- [14] X. J. Zhang, M. Xiao, Y. Cheng, M. H. Lu, and J. Christensen, Topological sound, *Commun. Phys.* **1**, 97 (2018).
- [15] G. C. Ma, M. Xiao, and C. T. Chan, Topological phases in acoustic and mechanical systems, *Nat. Rev. Phys.* **1**, 281 (2019).
- [16] Z. Zhang, H. Long, C. Liu, C. Shao, and J. Christensen, Deep-subwavelength hole acoustic second-order topological insulators, *Adv. Mater.* **31**, 1904682 (2019).
- [17] J. Y. Lu, C. Y. Qiu, L. P. Ye, X. Y. Fan, M. Z. Ke, F. Zhang, and Z. Y. Liu, Observation of topological valley transport of sound in sonic crystals, *Nat. Phys.* **13**, 369 (2017).
- [18] C. He, X. Ni, H. Ge, X. C. Sun, Y. B. Chen, M. H. Lu, X. P. Liu, and Y. F. Chen, Acoustic topological insulator and robust one-way sound transport, *Nat. Phys.* **12**, 1124 (2016).
- [19] L. Luo, H. X. Wang, Z. K. Lin, B. Jiang, Y. Wu, F. Li, and J. H. Jiang, Observation of a phononic higher-order Weyl semimetal, *Nat. Mater.* **20**, 794 (2021).
- [20] Q. Wei, X. W. Zhang, W. Y. Deng, J. Y. Lu, X. Q. Huang, M. Yan, G. Chen, Z. Y. Liu, and S. T. Jia, Higher-order topological semimetal in acoustic crystals, *Nat. Mater.* **20**, 812 (2021).
- [21] R. Suesstrunk and S. D. Huber, Observation of phononic helical edge states in a mechanical topological insulator, *Science* **349**, 47 (2015).
- [22] E. Prodan and C. Prodan, Topological Phonon Modes and their Role in Dynamic Instability of Microtubules, *Phys. Rev. Lett.* **103**, 248101 (2009).
- [23] S. F. Li, D. G. Zhao, H. Niu, X. F. Zhu, and J. F. Zang, Observation of elastic topological states in soft materials, *Nat. Commun.* **9**, 1370 (2018).
- [24] M. Miniaci, R. K. Pal, B. Morvan, and M. Ruzzene, Experimental Observation of Topologically Protected Helical Edge Modes in Patterned Elastic Plates, *Phys. Rev. X* **8**, 031074 (2018).
- [25] S. D. Huber, Topological mechanics, *Nat. Phys.* **12**, 621 (2016).
- [26] J. F. Zhao, C. W. Yang, W. T. Yuan, D. M. Zhang, Y. Long, Y. D. Pan, H. Chen, Z. Zhong, and J. Ren, Elastic Valley Spin Controlled Chiral Coupling in Topological Valley Phononic Crystals, *Phys. Rev. Lett.* **129**, 275501 (2022).
- [27] C. L. Ding, Y. B. Dong, Y. B. Wang, J. B. Shi, S. L. Zhai, and X. P. Zhao, Acoustic metamaterials and metasurfaces composed of meta-atoms and meta-molecules, *J. Phys. D: Appl. Phys.* **55**, 253002 (2022).
- [28] C. L. Ding, Y. B. Dong, and X. P. Zhao, Research advances in acoustic metamaterials and metasurface, *Acta Phys. Sin. (Beijing, China)* **67**, 194301 (2018).
- [29] H. J. Chen, H. Li, S. L. Zhai, C. L. Ding, L. M. Hao, C. R. Luo, and X. P. Zhao, Ultrasound acoustic metamaterials with double-negative parameters, *J. Appl. Phys.* **119**, 204902 (2016).
- [30] C. L. Ding, H. J. Chen, S. L. Zhai, and X. P. Zhao, Acoustic metamaterial based on multi-split hollow spheres, *Appl. Phys. A* **112**, 533 (2013).
- [31] Y. B. Wang, Y. B. Dong, S. L. Zhai, C. L. Ding, C. R. Luo, and X. P. Zhao, Tunable topological edge transport in acoustic meta-atoms, *J. Appl. Phys.* **128**, 234903 (2020).
- [32] Y. B. Wang, Y. B. Dong, S. L. Zhai, C. L. Ding, C. R. Luo, and X. P. Zhao, Reconfigurable topological transition in acoustic metamaterials, *Phys. Rev. B* **102**, 174107 (2020).
- [33] V. Peri, Z. D. Song, M. Serra-Garcial, P. Engeler, R. Queiroz, X. Huang, W. Deng, Z. Y. Liu, B. A. Bernevig, and S. D. Huber, Experimental characterization of fragile topology in an acoustic metamaterial, *Science* **367**, 797 (2020).
- [34] Y. B. Dong, Y. B. Wang, J. B. Shi, S. L. Zhai, C. L. Ding, and X. P. Zhao, Multiband acoustic topological metamaterials with valley-switchable higher-order corner states, *J. Phys. D: Appl. Phys.* **55**, 435301 (2022).
- [35] S. L. Zhai, H. J. Chen, C. L. Ding, and X. P. Zhao, Double-negative acoustic metamaterial based on meta-molecule, *J. Phys. D: Appl. Phys.* **46**, 475105 (2013).
- [36] M. B. de Paz, C. Devescovi, G. Giedke, J. J. Saenz, M. G. Vergniory, B. Bradlyn, D. Bercioux, and A. García-Etxarri, Tutorial: Computing topological invariants in 2D photonic crystals, *Adv. Quantum Technol.* **3**, 1900117 (2019).
- [37] N. Marzari and D. Vanderbilt, Maximally localized generalized Wannier functions for composite energy bands, *Phys. Rev. B* **56**, 12847 (1997).
- [38] T. C. Wu, X. Jiang, X. Wu, and Q. Han, Acoustic topological valley transport with multimode edge states, *J. Appl. Phys.* **130**, 124401 (2021).
- [39] H. Y. Fan, B. Y. Xia, L. Tong, S. J. Zheng, and D. J. Yu, Elastic Higher-Order Topological Insulator with Topologically Protected Corner States, *Phys. Rev. Lett.* **122**, 204301 (2019).
- [40] Z. Z. Yang, Y. Y. Peng, X. Li, X. Y. Zou, and J. C. Cheng, Boundary-dependent corner states in topological acoustic resonator array, *Appl. Phys. Lett.* **117**, 113501 (2020).